Full-Field Quantitative Determination of Strain and Stress Partitioning in Medium Mn TRIP Steels

Xiangbo Hu[1] · Chenghuan Liu[1] · Xiaogang Wang[1] · Chao Jiang[1]

Abstract

The aim of this paper is to present a new method for the quantitative determination of strain and stress partitioning in medium Mn transformation-induced plasticity (TRIP) steels with typical ferrite–austenite dual-phase microstructures. Firstly, based on scanning electron microscope (SEM) imaging, the strain field of the specimen surface during tensile deformation can be obtained using a developed microscopic digital image correlation (DIC) method. The different phases involving ferrite, austenite and nascent martensite after transformation are recognizable from the strain field, then the strain partitioning between phases can be solved experimentally. Secondly, regarding the stress partitioning, the constitutive models of the phases involved are established, and the relevant model parameters are identified using a proper regression method under the premise of the law of mixture and the iso-work law. Finally, strain and stress can be computed simultaneously at the phase level. The results show that there is significant inhomogeneity in the distribution of strain in different phases, as well as the distribution of stress. The proposed method allows providing valuable information for assessing the weight of different phases in contributing to the macroscopic mechanical properties of multi-phase steels, such as strength and ductility. This method can also be used to simulate the mechanical response of medium Mn TRIP steels at different austenite stabilities and different initial volume fractions of austenite, indicating therefore a great potential for improving material properties via microstructural tuning.

Keywords Medium Mn steels · Martensitic transformation · Digital image correlation · Strain partitioning · Stress partitioning

1 Introduction

In recent years, with increasing pressure from environmental protection and government regulations, modern vehicles are expected to be lighter and lighter. This, however, cannot be achieved as the expense of the safety of the vehicle. In this regard, the use of advanced high strength steels (AHSSs) as body-in-white provides an effective way to keep vehicles light and safe at the same time [1–7]. Among the large variety of AHSSs, the recently developed medium Mn

transformation-induced plasticity (TRIP) steel is considered a promising candidate. This new type of TRIP steel possesses a moderate content of Mn, typically 3–8 wt%. With its dedicatedly designed intercritical annealing process, it allows the retention of a large volume fraction of austenite (up to 65% or even higher) in the initial microstructure consisting of a ferrite matrix [8–11]. This retained austenite is metastable and prone to transform to martensite under tensile loading, resulting in a pronounced TRIP effect. This enables the simultaneous improvement of the tensile strength and ductility of the material [12–14]. As a result, most advanced medium Mn steels can achieve ultimate tensile strengths exceeding 1 GPa and uniform elongation above 30% [15–17].

Nevertheless, the potential of medium Mn steels is still huge, and the improvement of its mechanical properties through microstructure tailoring has been a continued concern in both academia and industry [18–22]. Extensive studies [23–27] have shown that intercritical annealing

✉ Xiaogang Wang
xgwang@hnu.edu.cn

✉ Chao Jiang
jiangc@hnu.edu.cn

1   State Key Laboratory of Advanced Design
    and Manufacturing Technology for Vehicle, College
    of Mechanical and Vehicle Engineering, Hunan University,
    Changsha 410082, China

parameters, especially temperature, may play an important role in tuning the microstructure, as the volume fraction and mechanical stability of retained austenite can be significantly changed during the intercritical annealing process. This will undoubtedly have a major impact on the macroscopic mechanical properties of the material formed. In fact, this change occurs not only in the content and stability of austenite, but also in the mechanical properties of austenite itself, as well as in its replacement martensite that is supposed to be formed by strain-induced martensitic transformation. The properties of the matrix ferrite will also be altered likewise during this process. Here, a key internal variable governing this heat treatment process is the redistribution of some essential elements such as Mn and C in different phases (i.e., chemical element partitioning) and their complex effects on sub-microstructures at different scales. This phenomenon has actually been concerned and studied extensively from a metallurgical point of view [28–30]. Nevertheless, relatively few studies have focused on its effect on the changes in the mechanical properties of the phases and their connection to the macroscopic mechanical behavior of the material as a multi-phase composite. This actually is the origin of the so-called strain partitioning (between phases) issue in medium Mn steels [20, 31–34]. The authors consider that, without properly addressing this issue, the mechanical behavior of medium Mn steels cannot be comprehensively understood, and the heat treatment will also lack effective guidance for the optimization of mechanical properties.

It is easy to recognize that the strain partitioning between the two phases ferrite and austenite in medium Mn steels is the norm but not exceptional because the two phases have different mechanical properties. Actually, due to their difference in hardness (or tensile strength), the two phases will not bear equal stress when the material is stretched, an issue of stress partitioning in the first place [15]. And then the strain produced by each phase should be consistent with its own constitutive relationship, which reflects the inherent mechanical properties of the phase. Nevertheless, deformation incompatibility between soft and hard phases is unavoidable in this process, which may generate internal stresses and complicate the final strain distribution [32, 35, 36]. Besides, another important variable for medium Mn steels is the expected transformation of austenite to martensite during deformation, which will bring about a new and generally very hard phase martensite. This may lead to significant changes in the initial stress/strain distribution.

A preliminary attempt to solve this problem is to assume that the stress is uniformly distributed in different phases, and then the strain of each phase can be estimated separately from its own constitutive relationship. Nevertheless, one can note that this method is too simplistic and can therefore only give a first guess. A more acceptable approach is to employ an iso-work assumption, which

presumes that the mechanical work increment of each phase remains equal during deformation [37–41]. And for each of the two variables, stress and strain, the law of mixture (i.e., the superposition principle) applies [39, 41]. This establishes a linkage between the mechanical behavior of the individual phases and that of the material as their ensemble. A key issue here is the construction of the constitutive model at the phase level and the correct identification of relevant model parameters. This is also often the difficulty in solving this problem, as there is no well-established method available for experimentally obtaining the stress–strain curve of an individual phase. Currently, a popular method is to estimate the stress and strain based on dislocation theories, since plastic deformation in alloys is predominantly provided by dislocation motion, and most strengthening mechanisms are effectuated by hindering dislocation motion [42–44]. In principle, this also applies to the medium Mn steel in question, provided that the additional effect of martensitic transformation is properly considered. However, the quantification of dislocations (e.g., dislocation density) and other relevant microstructural variables has been a long-standing challenging issue, making model verification a very difficult task.

In this work, the authors attempt to develop an alternative approach to identify stress/strain partitioning in duplex medium Mn steels. First, the strain partitioning between different phases is expected to be determined directly by experimental measurements, rather than using indirect methods based on microstructure characterization. This can be promisingly achieved by using a homemade microscopic DIC method based on SEM imaging, i.e., the SEM-DIC method, developed in our previous work [20]. This method enables in-situ full-field strain measurements at sub-grain and grain scales during tensile deformation. Second, the constitutive model of each phase needs to be constructed, and then based on the obtained information of strain partitioning and macroscopic stress–strain curve, a proper method needs to be developed that is expected to be able to identify all model parameters. Besides, the associated effect of martensitic transformation needs to be addressed separately. A major advantage of the above idea proposed is its simplicity. It is based on direct and accurate measurements of the strain field, avoiding therefore some strong assumptions and quantification of certain microstructural parameters that are often questionable. Moreover, the proposed approach can also provide practical guidance for improving the mechanical properties of medium Mn steels through microstructure optimization, for instance, by adjusting the volume fraction and stability of austenite which are all explicitly considered in the model. Hence, the proposed method can not only address the stress/strain partitioning at the phase level but also provide a means for the optimization of mechanical properties through microstructural tuning.

2 Material and Experiments

A medium Mn steel with chemical composition of Fe-7Mn-0.14C-0.23Si (wt%) is studied in this work. It has a dual-phase microstructure consisting of ferrite (α) and retained austenite (γ), as shown in Fig. 1a. The two phases have similar grain sizes, with an average value about 1 μm. An experimental analysis on Mn distribution in this material was conducted using energy dispersive spectroscopy (EDS) in Ref. [45]. It showed that there was a pronounced enrichment of Mn element in austenite, about 12 wt% against about 5 wt% in ferrite. This preferential Mn partitioning into austenite allows increasing its mechanical stability against transformation when it is subjected to tensile loading.

The macroscopic engineering stress–strain curve of the tensile specimen obtained at room temperature is displayed in Fig. 1b. It shows that the steel has an excellent combination of strength and ductility, with an ultimate tensile strength about 1030 MPa and uniform elongation about 36%. Here it is also worth noting that the plastic deformation of this material was accompanied with marked plastic instability phenomena, namely, the Lüders banding and Portevin-Le Châtelier (PLC) banding. They correspond to the stress plateau (Lüders stage) following the yield point and a series of serrations (PLC stage) during the work hardening, as labeled in the stress–strain curve in Fig. 1b. This phenomenon can be generally found in medium Mn steels [46–49]. Moreover, martensitic transformation occurred during plastic deformation, resulting in the birth of a new phase martensite (α'). This changed the material from an initial dual-phase steel to a triple-phase steel.

The SEM-DIC method was employed to measure the strain field of specimen surface during tensile deformation. A miniature plate dog-bone specimen with a gauge Section 2.5 mm × 8 mm and a thickness of 1 mm was adopted, and a tensile test was performed in situ using an SEM built-in servo-hydraulic testing equipment Shimadzu SEM-Servo Pulser. The model of the SEM was JEOL JSM-IT100

which enabled the highest resolution of 3 nm at 30 kV. The maximum force of the hydraulic cylinder was ± 10 kN (tension/compression), and the effective stroke of the piston was ± 10 mm. The tensile test was conducted in displacement-controlled mode with a constant crosshead velocity of 1 μm/s, corresponding to a macroscopic strain rate of 1.25×10^{-4} s^{-1}. During the tensile test, the SEM images of deforming specimen surface were recorded at different deformation stages (corresponding to macroscopic strains of 9.5%, 13.1%, 18.2% and 24.3%). These SEM images carrying deformation information were treated by using the developed SEM-DIC method [20], yielding respective displacement and strain fields as outcomes. The spatial resolution of the acquired SEM images was about 10 nm × 10 nm, allowing therefore finite deformation at sub-grain scales to be solved. Since the specimen surface was etched, phase boundaries information can be kept in the obtained strain fields, which enabled the full-field strain evaluation for individual phases.
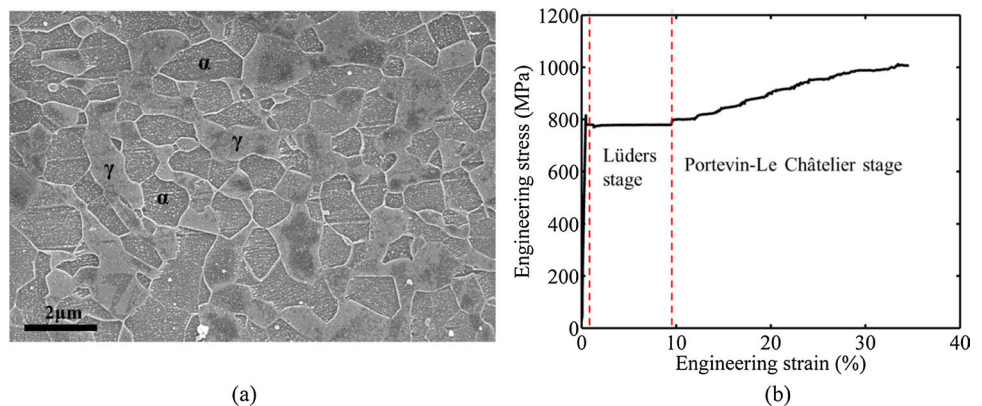
3 Method

3.1 Model Construction

The proposed method intends to solve the stress/strain partitioning in a multi-phase steel by establishing phase-level constitutive models and using experimental data obtained both at the phase scale and the macroscopic (specimen) scale. The steps of the model construction are presented below.

First, regarding the present multi-phase medium Mn steel in consideration, a correlation needs to be established between the stress and strain of each phase (α ferrite, γ austenite and α' martensite) and those of their ensemble, i.e., the macroscopic stress and strain of the material. To this end, a simple law of mixture assuming linear superposition is applied:

Fig. 1 **a** SEM image of the etched specimen surface showing a dual-phase microstructure of the studied medium Mn steel (α ferrite in dent and γ austenite in embossment). **b** Macroscopic engineering stress–strain curve of the specimen obtained in a quasi-static tensile test at room temperature

(a)

(b)

$$\sigma_{\mathrm{macro}} = f_\alpha \sigma_\alpha + f_\gamma \sigma_\gamma + f_{\alpha'} \sigma_{\alpha'} \tag{1}$$

$$\varepsilon_{\mathrm{macro}} = f_\alpha \varepsilon_\alpha + f_\gamma \varepsilon_\gamma + f_{\alpha'} \varepsilon_{\alpha'} \tag{2}$$

$$f_\alpha + f_\gamma + f_{\alpha'} = 1 \tag{3}$$

where σ_{macro} represents the macroscopic stress consisting of three components contributed by the three phases α, γ and α′. The stress components σ_α, σ_γ and $\sigma_{\alpha'}$ stand for the stresses of the respective phases, and f_α, f_γ and $f_{\alpha'}$ are their corresponding volume fractions in the material. Analogously, $\varepsilon_{\mathrm{macro}}$ represents the macroscopic strain, and ε_α, ε_γ and $\varepsilon_{\alpha'}$ represent the strains of the respective phases.

Second, the constitutive relationship of the individual phases needs to be established by correlating stress and strain. In this work, a common power law is applied, expressed as below:

$$\sigma_i = \sigma_{y,i} + h_i \varepsilon_i^{m_i} \tag{4}$$

where σ_i and ε_i represent the stress and strain of phase i (α/γ/α′), respectively. $\sigma_{y,i}$ represents the yield strength of phase i, and h_i and m_i stand for the phase-dependent parameters characterizing the work hardening behavior of phase i.

In this work, the yield strengths of individual phases are estimated by considering the solid solution strengthening effect and grain boundary strengthening effect, two major strengthening effects for the studied medium Mn steel. According to the literature [37], the following formula can be used to estimate the yield strength of each phase:

$$\sigma_{y,\alpha} = 5000 X_\alpha^{\mathrm{C}} + 44.7 X_\alpha^{\mathrm{Mn}} + 138.6 X_\alpha^{\mathrm{Si}} + \frac{K_\alpha}{\sqrt{\mathrm{d}_\alpha}} \tag{5}$$

$$\sigma_{y,\gamma} = 567 X_\gamma^{\mathrm{C}} - 1.5 X_\gamma^{\mathrm{Mn}} + 23 X_\gamma^{\mathrm{Si}} + \frac{K_\gamma}{\sqrt{\mathrm{d}_\gamma}} \tag{6}$$

$$\sigma_{y,\alpha'} = 1720 X_{\alpha'}^{C} + 413 \tag{7}$$

where X_i^{C}, X_i^{Mn} and X_i^{Si} are the mass fractions of the elements C, Mn and Si in phase i, respectively. The parameter K_i represents the Hall–Petch parameter of phase i, and d_i represents the average grain size of phase i. It is worth noting that the solid solution of C in martensite is the dominant factor affecting the yield strength of martensite, such that the effects of other elements (e.g., Mn and Si) and grain boundaries were ignored in Eq. (6).

The SEM-DIC method employed allows quantitative assessment of the strain in individual phases, including ferrite, austenite and martensite. In the displacement-controlled tensile test (at constant strain rate) of the studied medium Mn steel, a general linear increase trend can be found in ferrite and martensite, while austenite shows a nonlinear increase trend. Then the relationships between the strain in individual phases and the macroscopic strain can be established as follows:

$$\varepsilon_\alpha = k_\alpha \varepsilon_{\mathrm{macro}} \tag{8}$$

$$\varepsilon_{\alpha'} = k_{\alpha'} \varepsilon_{\mathrm{macro}} \tag{9}$$

$$\varepsilon_\gamma = k_\gamma (\varepsilon_{\mathrm{macro}})^{n_\gamma} \tag{10}$$

where k_α, $k_{\alpha'}$, k_γ and n_γ are parameters related to the strain evolution of ferrite, martensite and austenite, which can be determined by the SEM-DIC method in a tensile test.

It is necessary to note that the strain of martensite $\varepsilon_{\alpha'}$ defined in this work is actually constituted of three components, which include the strain of its parent phase austenite $\varepsilon_{\gamma,a}$ before transformation, the strain due to TRIP effect (commonly called TRIP strain [50]) ε_{TP} during transformation and the strain of martensite itself $\varepsilon_{\alpha',p}$ after transformation, i.e.,

$$\varepsilon_{\alpha'} = \varepsilon_\gamma + \varepsilon_{TP} + \varepsilon_{\alpha',p} \tag{11}$$

Here it is important to emphasize that two terms $\varepsilon_{\alpha'}$ and $\varepsilon_{\alpha',p}$ represent different quantities. The former represents the total accumulated strain of martensite counted from the very beginning before the transformation, and the latter represents only the pure strain of martensite counted from the occurrence of the transformation. For the convenience of expression, the strain term $\varepsilon_{\alpha',p}$ is called the strain of pure martensite to distinguish it from the strain of martensite $\varepsilon_{\alpha'}$ which takes into account the deformation history before it becomes martensite.

Since the martensitic transformation in consideration is a strain-induced transformation, it is reasonable to assume there is a critical strain triggering the transformation, denoted $\varepsilon_{\gamma,c}$. Then Eq. (11) can be rewritten by:

$$\varepsilon_{\alpha'} = \varepsilon_{\gamma,c} + \varepsilon_{TP} + \varepsilon_{\alpha',p} \tag{12}$$

The TRIP strain can be estimated according to Ref. [50], which considers both the accommodation effect (Greenwood-Johnson effect) and the orientation effect (Magee effect) of the martensitic transformation. It shows that the TRIP strain ε_{TP} is proportional to the volume fraction of martensite $f_{\alpha'}$, and each unit volume fraction of martensite can induce 4.7% TRIP strain, namely:

$$\varepsilon_{TP} = 0.047 f_{\alpha'} \tag{13}$$

The volume fraction of martensite $f_{\alpha'}$ can be estimated using a classical Olson-Cohen model [51], i.e.,

$$f_{\alpha'} = f_{\gamma 0}\left\{1 - \exp\left[-\beta\left[1 - \exp\left(-\alpha\varepsilon_{\mathrm{macro}}\right)\right]^n\right]\right\} \tag{14}$$

where $f_{\gamma 0}$ represents the initial volume fraction of austenite, α, β and n represent the material constants characterizing the martensitic transformation kinetics.

Thanks to the full-field strain measurement by SEM-DIC, the strains of ferrite, austenite and martensite can be obtained directly, while the strain of pure martensite can be estimated according to the above equations. Now the main concern is the solution of the stresses of the individual phases. The approach employed in this work is to resort to the constitutive models of individual phases established in Eq. (4). To do so, the relevant work hardening parameters in the models, namely, h_i and m_i, need to be identified. Based on the macroscopic mechanical response of the material and the premise of the law of mixture, a regression analysis was employed in this work.

Regarding the macroscopic stress σ_{macro}, the difference between its experimental value $\sigma_{\mathrm{macro, exp}}$ derived from the macroscopic stress–strain curve and a theoretical estimate by Eq. (4) (denoted $\sigma_{\mathrm{macro, est}}$) needs to be introduced:

$$r\left(h_i, m_i\right) = \sigma_{\mathrm{macro, est}}\left(h_i, m_i\right) - \sigma_{\mathrm{macro, exp}} \tag{15}$$

By using the least squares method, the objective function to be optimized can be expressed as:

$$R\left(h_i, m_i\right) = \sum r^2\left(h_i, m_i\right) \tag{16}$$

Then, using the Gauss–Newton method, the parameters h_i and m_i can be obtained when the objective function takes the minimum value $R_{\min}$:

$$R_{\min} = \min\left[R\left(h_i, m_i\right)\right] \tag{17}$$

Here it is important to note that the iso-work law is implicit in the above solution process, which is used as a constraint for parameter optimization. The iso-work law simply assumes that mechanical work contributed by each phase is equal. More specially, considering the state before and after transformation, one can obtain the following equation:

$$\sigma_\alpha d\varepsilon_\alpha = \sigma_\gamma d\varepsilon_\gamma = \sigma_{\alpha'} d\varepsilon_{\alpha'} \tag{18}$$

The above is the presentation of the methodology proposed for the solution of stress/strain partitioning between phases. Next, the identification of the relevant model parameters involved in this method is presented below.

3.2 Model Parameters Identification

First, the volume fraction of martensite in the material can be determined quantitatively by using X-ray diffraction (XRD). As presented in Ref. [43], when specimens deformed at different strain levels were measured by XRD, the evolution
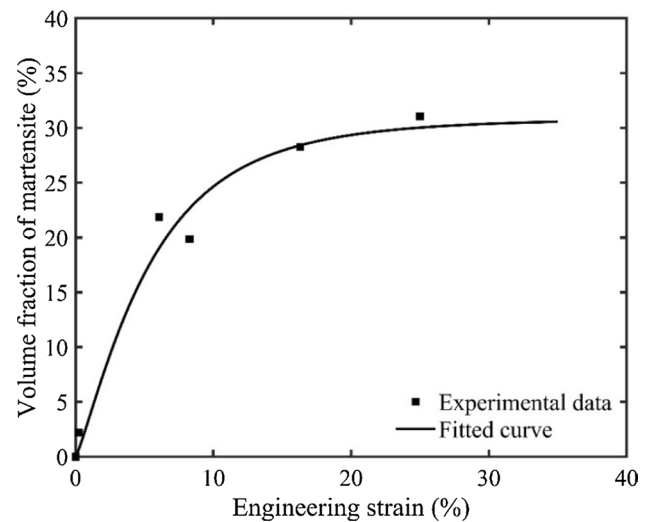

Fig. 2 Evolution of volume fraction of martensite as a function of macroscopic strain in a tensile test: experimental data (extracted from Ref. [52]) versus fitted curve by the Olson-Cohen model

Table 1 Calibrated Olson-Cohen model parameters for the studied material

$f_{\gamma 0}$	α	β	n
30%	4	6	1.2

of the martensitic transformation during tensile testing can be assessed, as the experimental data plotted in Fig. 2. The data can be fitted into a curve representing the relationship between the volume fraction of martensite and the macroscopic engineering strain described by the Olson-Cohen model, as shown in Fig. 2. The relevant model parameters are reported in Table 1. The results show that the martensitic transformation in the present steel occurs mostly at early stages of deformation, and then enters saturation quickly (at a strain level about 16%). This transformation kinetics is well represented by the Olson-Cohen model.

Here, another important parameter related to the transformation, namely the triggering strain to transformation $\varepsilon_{\gamma,c}$, needs to be determined. This can be realized via an optimization approach, where an optimal $\varepsilon_{\gamma,c}$ is sought. The procedure is as follows. For a given $\varepsilon_{\gamma,c}$, the volume fraction of austenite f_γ can be estimated alternatively (different from the above approach) from the strain field obtained by DIC, since prior-austenite grains with strain values below $\varepsilon_{\gamma,c}$ can be identified as untransformed austenite (and vice versa, martensite after transformation). The f_γ thus obtained is then expected to approximate the f_γ value given by the established Olson-Cohen model at the same strain level, since the latter is validated by XRD measurements. This can be readily solved by optimization to find the optimal $\varepsilon_{\gamma,c}$. It was determined to be 7.3%, as the mean value of the estimates from the strain fields available in this work.

Fig. 3 **a** Evolution of strain of individual phases as a function of macroscopic strain. **b** Decomposition of strain of martensite phase into three components (austenite, pure martensite and TRIP) and their evolution with macroscopic strain
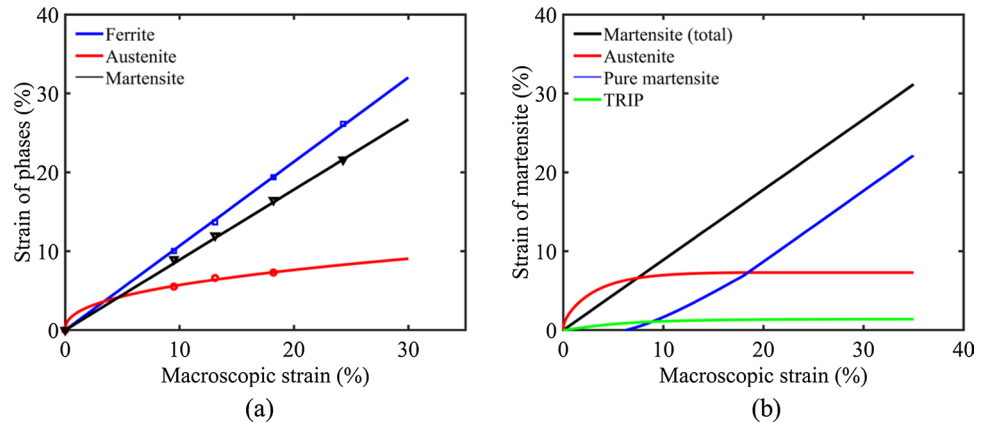

(a)

(b)

Table 2 Calibrated parameters k_i and n_i of phases

Phase	α	γ	α′
k_i	1.067	0.15	0.89
n_i	N/A	0.42	N/A

Second, concerning the strain evolution, the average strain of each phase can be estimated directly from the strain fields obtained by SEM-DIC. And then they can be correlated to the macroscopic strain following established relationships according to Eqs. (8)–(10), as shown in Fig. 3a. The relevant parameters k_i and n_i estimated are reported in Table 2.

The strain of martensite phase can be further decomposed into three components according to Eq. (11), namely, the strain of austenite ε_γ, the strain of pure martensite $\varepsilon_{\alpha',p}$ and the TRIP strain ε_{TP}. The strain of austenite ε_γ can be estimated directly using Eq. (10), and the TRIP strain ε_{TP} can be estimated using relationships in Eqs. (13) and (14). Then, according to Eq. (12), the strain of pure martensite $\varepsilon_{\alpha',p}$ can be calculated by subtracting $\varepsilon_{\gamma,c}$ (consistently equal to 7.3%) and ε_{TP} from the total strain of martensite $\varepsilon_{\alpha'}$ estimated from Eq. (9). The results obtained are illustrated in Fig. 3b. It shows that the contribution of strain from austenite is significant in the early stage of deformation and then saturates as the martensitic transformation is completed. The contribution of martensite itself becomes more and more important as a greater volume fraction of the material transforms to martensite. And it also indicates that TRIP is not a significant contributor to strain in the studied material.

The yield stress of each phase can be estimated according to Eqs. (5)–(7) based on the chemical composition and grain size of the phase. The obtained results are listed in Table 3. Then the hardening parameters in the constitutive models of phases can be calibrated using the method presented above, and the obtained results are reported in Table 4.

To this point, all the parameters involved in the proposed method have been calibrated. The calibrated constitutive models can then be used to plot the macroscopic engineering stress–strain curve. The plotted curve is shown in Fig. 4a, where the true curve obtained experimentally is also displayed for comparison. One can note that the two curves overlap very well, which demonstrates the effectiveness of the calibrated models from at least a macroscopic point of view. The modelled stress–strain relationships of individual phases involved in the studied material are illustrated in Fig. 4b. It clearly shows that there are large differences in the strength and ductility of the different phases. In particular, the martensite phase exhibits distinct mechanical behavior from its parent phase austenite and the matrix ferrite. This explains well why understanding the material behavior at the phase level is so important for multi-phase materials, especially when phase transformations are involved and play an important role. It is worth noting here that an implicit

Table 4 Calibrated hardening parameters in the constitutive models of phases

Phase	h_i	m_i
α	550	0.67
γ	450	0.50
α′	850	0.75

Table 3 Calibrated parameters related to yield strengths of phases

Phase	X_C (wt%)	X_{Mn} (wt%)	X_{Si} (wt%)	K (MPa m$^{1/2}$)	d (μm)	$\sigma_{y,i}$ (MPa)
α	0.02	5	0.23	180	1.0	526
γ	0.42	12	0.23	240	1.2	465
α′	0.42	N/A	N/A	N/A	N/A	1135

Fig. 4 **a** Comparison of two macroscopic stress–strain curves obtained from experiment and modelling, respectively. **b** Modelled stress–strain curves of individual phases including ferrite, austenite and martensite
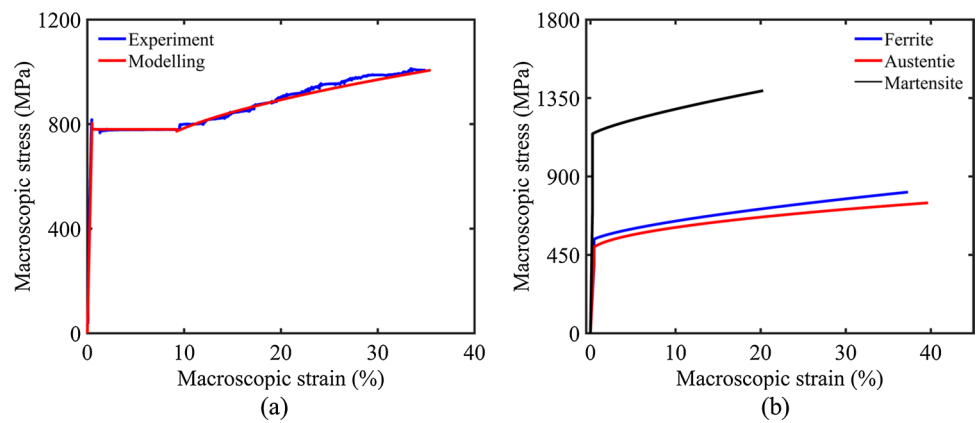
assumption made in the modelling is that when the stretched material reaches its breaking point in a tensile test, both ferrite and martensite break at that point (all austenite had been transformed to martensite before this moment). This is actually consistent with the fracture observations in the experiment. The results and understanding gained from the established models are presented in the following sections.

4 Results

The strain field evolution of specimen surface during tensile deformation were obtained in situ thanks to the developed SEM-DIC method. Some representative experimental results are shown in Fig. 5, which exhibits a sequence of strain fields at selected moments (corresponding to macroscopic strain levels 9.5%, 13.1%, 18.2% and 24.3%) during the tensile test. Different phases can be identified from the displayed strain fields since α ferrite is in dent and γ austenite is in embossment. The phase transformation from γ austenite to α′ martensite can be determined simply according to whether the strain of the grain exceed the critical strain $\varepsilon_{\gamma,c}$ triggering martensitic transformation. For a clearer presentation, the symbols of the different phases are marked in the strain fields in Fig. 5, especially with the γ austenite circled in yellow.

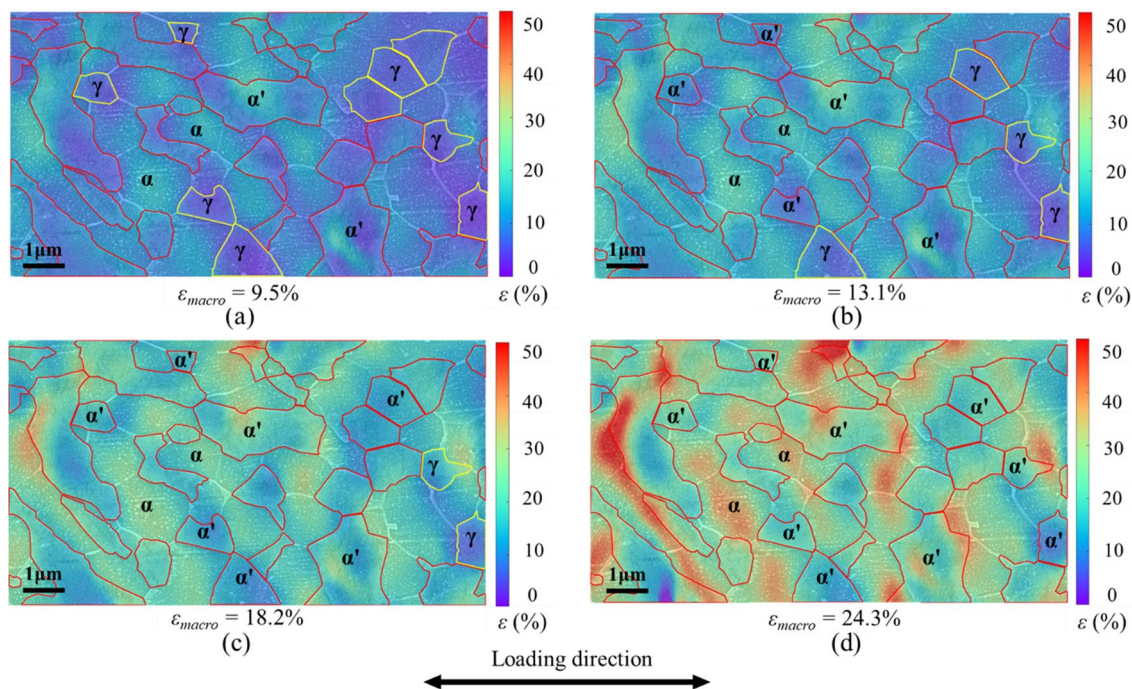From the strain fields one can first remark that the strain distribution is inhomogeneous. Different phases show

Fig. 5 A sequence of strain fields at selected moments (corresponding to macroscopic strains 9.5%, 13.1%, 18.2% and 24.3%) during the tensile deformation

different strain levels. More specifically, α ferrite exhibits considerably higher strains than its counterpart γ austenite (lighter colors in the image indicate higher strains), and when γ austenite is replaced by α′ martensite, this situation has changed somewhat, but not substantially. One can also note that this strain heterogeneity is manifested not only at the phase level but also at the grain level, i.e., even for the same phase, different grains exhibit different strain levels. Nevertheless, despite the strong strain heterogeneity, the strain distribution pattern does not change much throughout the deformation process. Regarding the source of strain heterogeneity, further quantitative analysis was conducted at the grain level, and the statistical results of strain of individual grains in different phases and their evolution during the test (at the same moments with the strain fields in Fig. 5) are illustrated in Fig. 6. The average strains of phases are also provided in the images, as shown by the dashed lines.

For each of the three phases involved, grain-level strain heterogeneity is clearly shown in Fig. 6, which is reflected in the large fluctuations of the strain of grains. This diversity can partially be explained by differences in grain size, grain orientation and other possible variables at the grain level. The heterogeneity of dislocation density distribution among different grains may also play an important role, as discussed in detail in [25]. Nevertheless, the more important information provided by Fig. 6 is that there exist substantial differences in the strain levels of the different phases, which

are systemically exhibited during tensile deformation. More specifically, ferrite consistently demonstrates the highest strain level, which is higher than that of martensite and much higher than that of austenite. The low strain level of austenite can be reasonably understood as martensitic transformation occurs rapidly in the early stages of deformation, as shown in Fig. 2. After martensitic transformation, the strain of the austenite is transferred to the transformed martensite, which also benefits from the TRIP effect. Even so, the martensite still shows a lower strain than the ferrite at the completion of all phase transformation (at macroscopic strain of 24.3%), namely 21.6% vs. 26.2%, as shown in Fig. 6d. Actually, the contribution of individual phases to the total strain can be assessed by introducing a concept of strain contribution ratio μ_ε, which can be defined by the following form for a specific phase i:

$$\mu_\varepsilon = \varepsilon_i f_i / \varepsilon_{\text{macro}} \tag{19}$$

The above equation shows that the strain contribution ratio depends both on the strain level of the phase and its volume fraction in the material. According to this definition, the strain contribution ratio of different phases can be evaluated, and its evolution with macroscopic strain is plotted, as shown in Fig. 7. It shows that the contribution ratio of ferrite is as high as 74%, which is constant during the entire deformation process. This is due to the fact that the strain

Fig. 6 Evolution of strain of grains in different phases (ferrite, austenite and martensite) at different macroscopic strain levels corresponding to the strain fields in Fig. 5
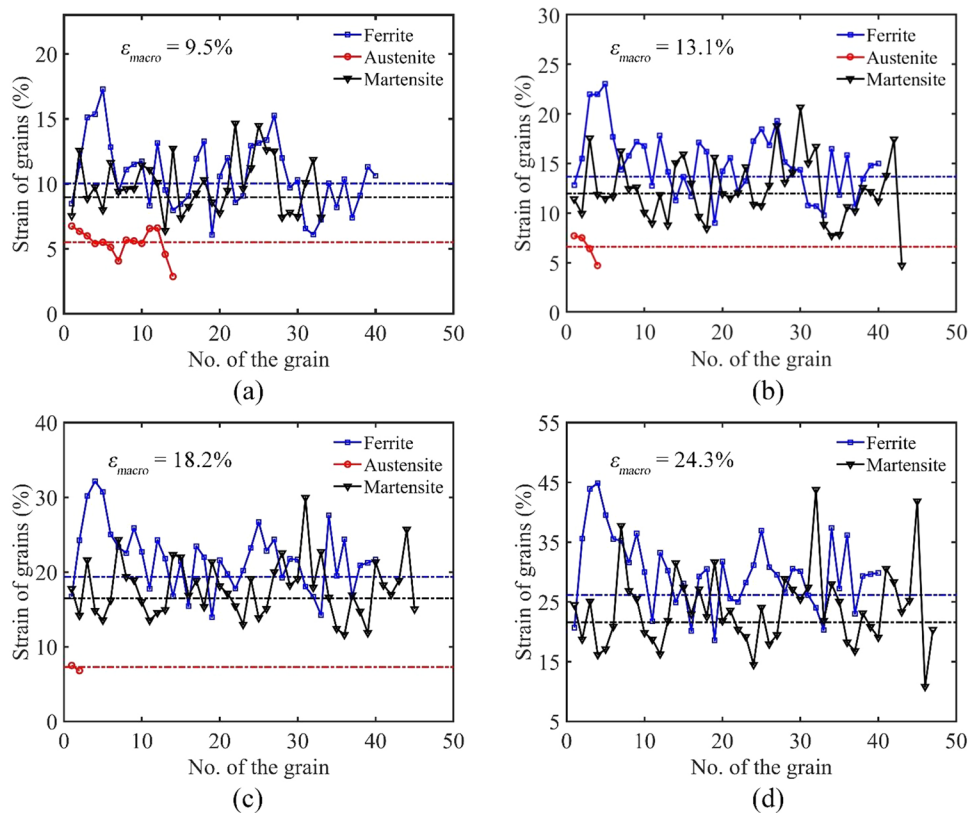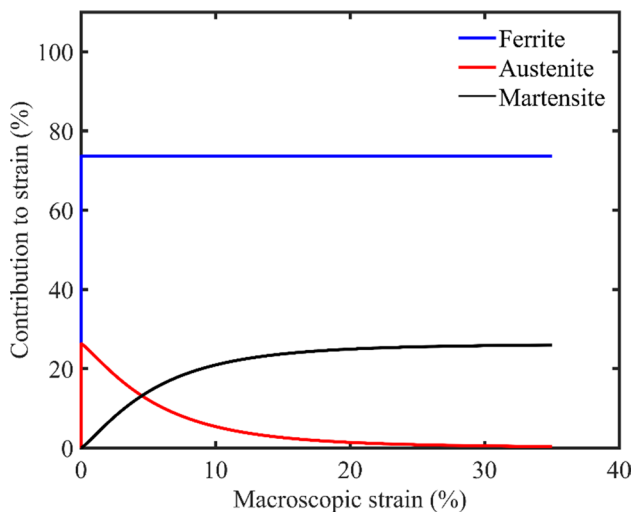
Fig. 7 Evolution of strain contribution ratio of different phases involved (ferrite, austenite and martensite) with macroscopic strain in a tensile test

of ferrite evolves linearly with the macroscopic strain (then $\varepsilon_\alpha/\varepsilon_{macro}$ in Eq. 19 is a constant), and the volume fraction of ferrite f_α keeps constant (about 70%) during tensile deformation. It can be noted that, in addition to the good ductility of ferrite as demonstrated above, the high volume fraction of ferrite also plays an important role in the final high strain contribution of ferrite to the total strain. Austenite and martensite contribute a total of 26% to the macroscopic strain, and their respective contributions shows exactly opposite evolution trends due to the change of volume fraction caused by phase transformation. In fact, as early as around 10% macroscopic strain, martensite dominates the austenite–martensite complex in terms of strain contribution as most of the phase transformation has been completed. Nevertheless, its contribution is still considerably lower than that of ferrite. The strain contribution ratio of the latter is about 2.8 times that of the former. It is also worth noting here that although austenite is a soft and ductile phase in the studied material (as shown in Fig. 4b), its high ductility is actually severely limited due to the rapid and extensive martensitic transformation occurred at the early stages of tensile deformation. As a result, its strain contribution is insignificant during most of the tensile test (except for the very beginning), as shown in Fig. 7.

Based on the strain fields obtained from SEM-DIC measurements, the stress fields can be evaluated in a straightforward way by using the constitutive models of the individual phases involved. Figure 8 exhibits a sequence of stress fields evaluated by this method, which have a one-to-one correspondence with the strain fields shown in Fig. 5. It can be clearly seen that the present stress fields demonstrate much more differences between phases than the strain fields. Generally, the three different phases involved can be roughly distinguished from three different colors in Fig. 8: austenite grains are in blue (low stress level, generally below 590 MPa), ferrite grains are in green (moderate stress level, generally at 610 MPa to 850 MPa), and martensite grains are in red (high stress level, generally above 1200 MPa). This pronounced stress partitioning effect is, in essence, due to the significant difference in mechanical properties between the different phases. It is now interesting to quantify the stress contributions of the different phases and their evolution with macroscopic strain.

A parameter similar to the strain contribution measure is adopted here, that is, the stress contribution ratio μ_σ. It can be evaluated for a specific phase i by:

$$\mu_\sigma = \sigma_i f_i \big/ \sigma_{macro} \qquad (20)$$

According to the above equation, the stress contribution ratio of each phase is assessed over the tensile test, and the results obtained are illustrated in Fig. 9. First, it can be noted that the austenite phase does not play an important role from the perspective of the overall deformation history. While its initial value is relatively high at about 28% at the beginning of deformation, it rapidly drops to considerably low levels as extensive martensitic transformation takes place (before a macroscopic strain of 10%), and then becomes almost negligible. In contrast, the other two phases of ferrite and martensite are the main active elements contributing to the macroscopic stress. The contribution of ferrite is as high as 72% at the beginning and then gradually decreases to a plateau of about 58% for the most part of the tensile test. The predominance of ferrite is, to a large extent, due to its high volume fraction. The stress contribution of martensite is also important. It increases rapidly with the transformation and stabilizes at a level of about 42% for the remaining main part of the deformation. This is remarkable considering the fact that the maximum volume fraction of martensite is only about 30%. Its stress contribution per volume fraction is higher than that of ferrite (about 1.7 times) due to its most salient mechanical feature, namely its ultrahigh hardness.

The above analysis shows that the ferrite phase makes the most important contribution in terms of both strain and stress. The role of martensite is also important, especially in terms of stress, whereas the role of austenite is not significant. It should be emphasized here that this conclusion is only applicable to the present material with its specific phase composition and characteristics. First, it has a high proportion of ferrite and a relatively low proportion of initial austenite. This may reduce the potential contribution of martensite (especially in terms of stress) due to the apparent constraint on volume. Second, the low mechanical stability of austenite in the present material leads to martensite transformation early in deformation. This means the early
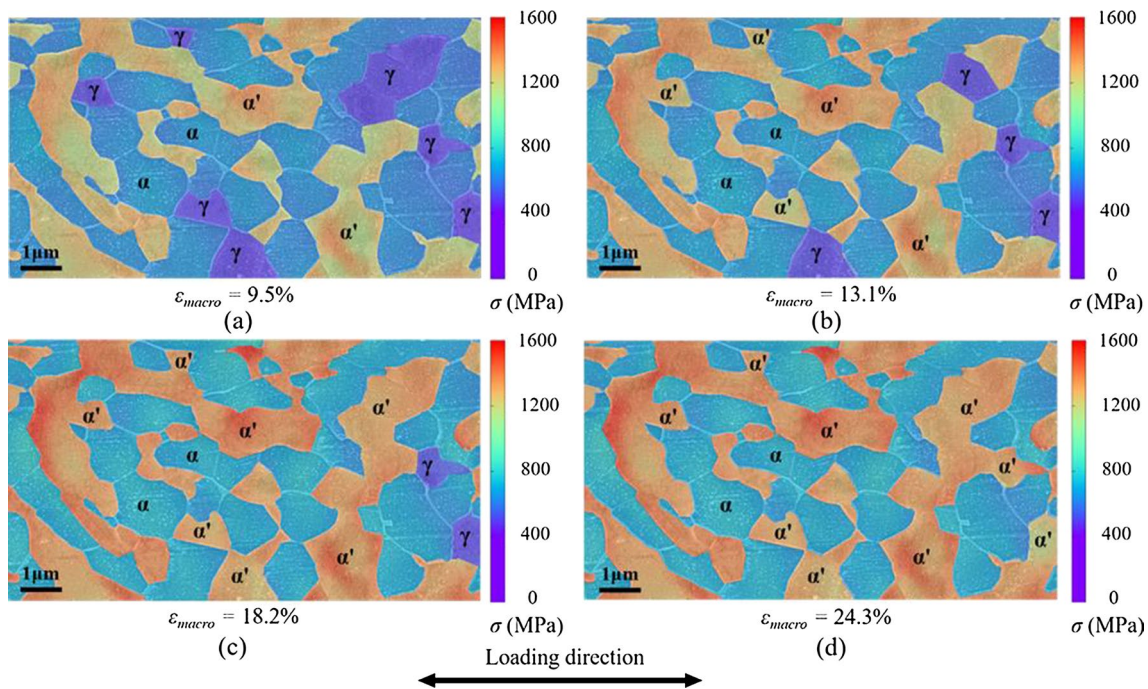
Fig. 8 A sequence of stress fields evaluated by the proposed method at different macroscopic strain levels corresponding to the strain fields in Fig. 5

activation of the effect of martensite (e.g., high hardness but low ductility) at the expense of the effect of austenite (e.g., high ductility). Hence, it can be learned that the volume fraction of austenite (or conversely that of ferrite) and its stability are two important variables that can affect the overall mechanical properties of the material in a significant way. Then it is intriguing to quantitatively evaluate the

Fig. 9 Evolution of stress contribution ratio of different phases involved (ferrite, austenite and martensite) with macroscopic strain in a tensile test

influence of these two variables on the macroscopic mechanical behavior, as an effort to optimize material properties. It is elaborated in the following section.

5 Discussions

First, the influence of the initial volume fraction (VF) of austenite on the mechanical properties of the material, namely the ultimate tensile strength (UTS) and uniform elongation (UE), was investigated. In this regard, the product of strength and elongation (PSE) was also considered an effective measure of overall mechanical properties of the material. The adjustment of the VF can be realized simply by changing the parameter $f_{\gamma 0}$ in the Olson-Cohen model (Eq. 14), and the selected investigation range in this work was 20%–40%. Another important parameter β in the Olson-Cohen model characterizing the stability of austenite was set to a fixed value of 6, which was the same as that of the studied material in this work. Other relevant material parameters were also kept consistent with the studied material. Then five cases with different VF (20%, 25%, 30%, 35%, and 40%) were selected for analysis. It is worthy to note that the case of VF-30% corresponds to the studied material in this work. The martensitic transformation kinetics in the five analysed cases is shown in Fig. 10a, and the estimated results of UTS, UE and PSE are shown in Fig. 10b–d in turn.
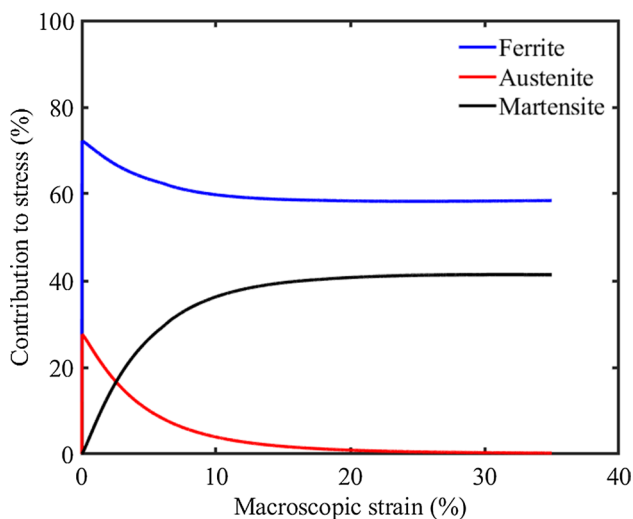
Fig. 10 Influence of different VF of initial austenite (from 20 to 40%) on the mechanical properties of the material: **a** Evolution of VF of martensite with macroscopic strain assessed by the Olson-Cohen model. **b** Estimated UTS versus VF of initial austenite. **c** Estimated UE versus VF of initial austenite. **d** Estimated PSE versus VF of initial austenite
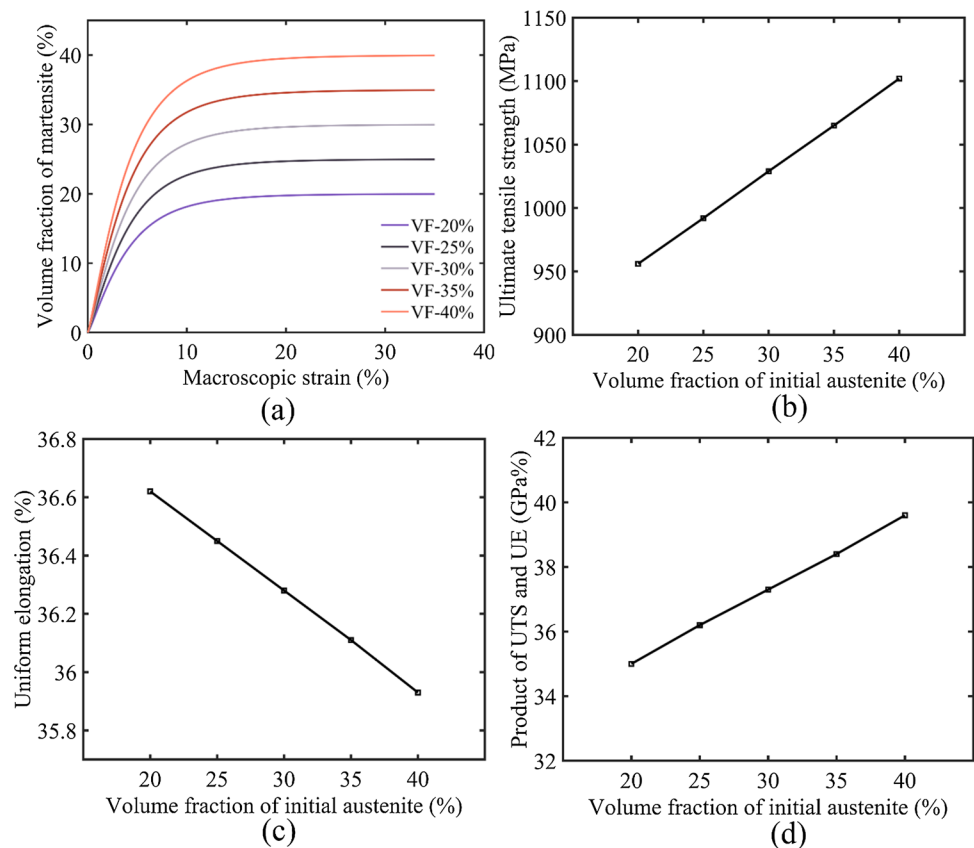

Figure 10a shows that at the same macroscopic strain, the case with higher VF of initial austenite produces more transformed martensite. Nevertheless, the five analysed cases exhibit similar transformation kinetics: martensitic transformation occurs rapidly with deformation and soon reaches a saturation stage (after about 10%–15% macroscopic strain) where almost all of the austenite is transformed. The strength estimates shown in Fig. 10b demonstrate that the UTS increases rapidly and quasi-linearly with the VF of austenite. For every 5% increase in VF of austenite, UTS increases by nearly 4%. This significant increase is due to a corresponding increase of transformed martensite (in the case of higher VF of initial austenite), which has been shown to be a major contributor to strength in the above analysis. In terms of ductility, Fig. 10c shows that the estimated UE decreases with the VF of austenite. The magnitude of the decline, however, is not significant. For every 5% increase in VF of austenite, UE decreases only by about 0.5%. Therefore, unlike the strength, ductility is not sensitive to the VF of austenite. A plausible explanation for this is that the strain contribution by the transformed martensite is offset by the reduction in the VF of ferrite (due to the increase in the VF of initial austenite), which is a more efficient contributor to strain as a soft phase, as demonstrated above. Then, considering the combination of strength and ductility, it is rather

straightforward that the PSE will follow almost the same evolution trend as UTS, as shown in Fig. 10d.

Regarding the other important variable, the austenite stability, the parameter β in the Olson-Cohen model was adjusted to tune the transformation tendency of the material. Five cases with different β (0.5, 1.5, 3, 6, and 9) with the same initial austenite VF of 30% (the present material) were chosen for investigation. High β values indicate a higher transformation tendency and therefore lower austenite stability. The evaluated martensitic transformation kinetics is shown in Fig. 11a, and the estimates of UTS, UE and PSE are shown in Figs. 11b–d in turn. Figure 11a shows that the austenite stability affects the transformation rate as well as the final VF of transformed martensite. For cases of low transformation tendency (e.g., $\beta = 0.5$, 1.5, and 3), only a part, but not all, of the austenite is transformed to martensite. The strength estimates in Fig. 11b exhibit that the UTS generally grows with the transformation tendency of austenite. This can be attributed to the beneficial effect of transformed martensite on strength. It can be also noted that this strengthening effect is more pronounced for austenite with high stability (i.e., lower β value), as this can cause a significant difference in the amount of martensite formed, as demonstrated in Fig. 11a. Whereas for cases with low stable austenite (e.g., β higher than 3), the gap between their UTS becomes much smaller

Fig. 11 Influence of different mechanical stability of initial austenite (with β varying from 0.5 to 9) on the mechanical properties of the material: **a** Evolution of VF of martensite with macroscopic strain assessed by the Olson-Cohen model. **b** Estimated UTS versus stability of initial austenite. **c** Estimated UE versus stability of initial austenite. **d** Estimated PSE versus stability of initial austenite
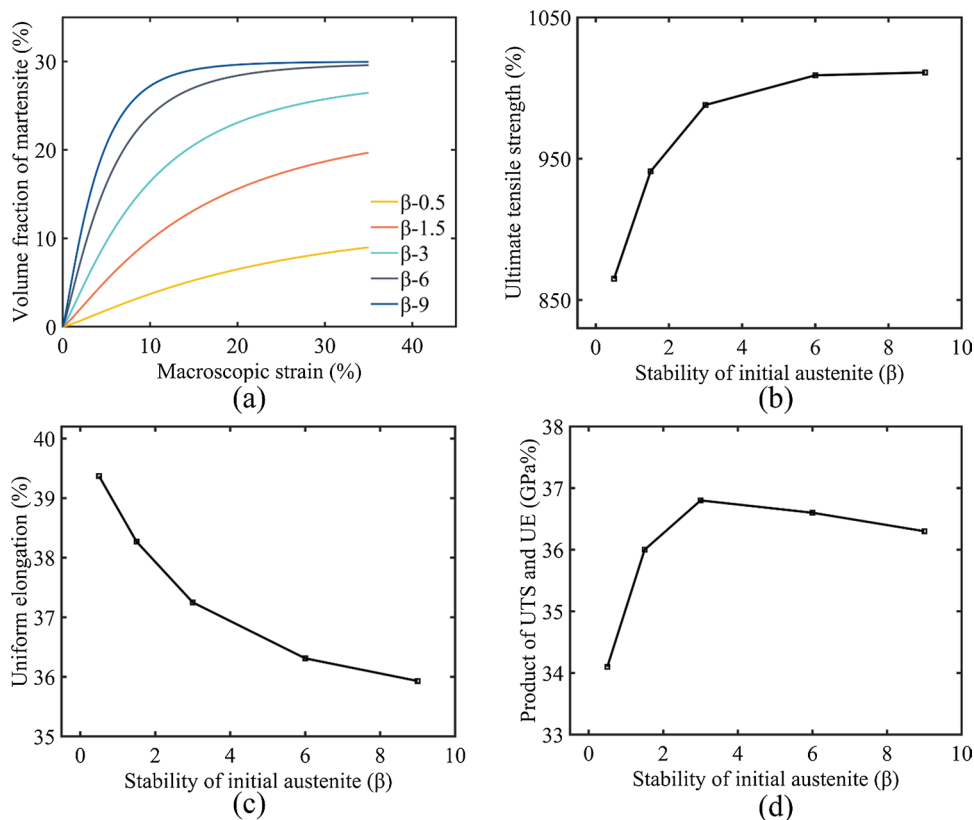
as almost all the initial austenite will be transformed to martensite at the end of the tensile test, although their transformation rates are different. Figure 11c shows that the UE follows a general decreasing trend with the transformation tendency of austenite, and the decreasing rate is apparently higher at the initial stage with low transformation tendency (β below 3). This result can be reasonably explained by acknowledging the fact that the soft austenite has a large potential for strain contribution while the hard martensite has a very limited contribution to strain. A slow transformation process (corresponding to a lower transformation tendency) makes better use of the deformability of the austenite before it is replaced by martensite. Earlier and more martensite formation plays the opposite role. One can note from Fig. 11b and c that for the selected range of austenite stability, UST varies from 865 to 1010 MPa and UE varies from 39.3 to 35.9%. The variation range of UST is about 145 MPa (increasing) and that of UE is about 3.4% (decreasing). Then considering these two opposite evolution trends, their resulting PSE shown in Fig. 11d demonstrates non-monotonic evolution with β. The estimated PSE increases rapidly at first and then declines slowly as the transformation tendency increases. The maximum value of PSE can be found when β is equal to 3. It can be considered as an optimal choice for austenite stability, provided that PSE is regarded as an indicator to evaluate the mechanical properties of the material.

The analysis above shows that the proposed method can provide a useful tool to evaluate the influence of the amount and stability of austenite on the macroscopic material behavior. The results indicate that, in general, as the VF of initial austenite increases, better strength can be obtained with a slight loss of ductility. And as the stability of austenite decreases, the strength of the material can be improved as the expense of reduced ductility. A better combination of strength and ductility is expected to be achieved by engineering a higher volume fraction of austenite with appropriate stability in the initial microstructure of medium Mn steels.

6 Conclusions

In this paper, the issue of strain and stress partitioning at the phase level in medium Mn steels is comprehensively investigated. The main concluding remarks are as follows.

First, an innovative experiment-modelling combined approach is proposed that enables the quantitative determination of the strain and stress fields of specimen surface subjected to tensile deformation. The full-field strain is assessed experimentally using the SEM-DIC method, and the stress distribution is evaluated based on the obtained strain fields and the constitutive models of the phases involved. In terms of technical feasibility, this method successfully actualizes the quantitative assessment of stress and strain partitioning

at the phase and even grain level in multi-phase polycrystalline materials.

Second, the stress and strain partitioning of different phases involved in the studied medium Mn steel, namely ferrite, austenite and martensite, is systematically analyzed. Due to its dominance in volume fraction, the ferrite turns out to be the most important contributor in both strain and stress. The martensitic transformation, however, is shown to be a critical variable that may considerably affect the mechanical properties of the material. In particular, the transformed martensite contributes significantly to strength, while the initial austenite may also play a role in strain contribution.

Third, the volume fraction and stability of austenite are considered and analyzed as two variables affecting the mechanical properties of the material. The analysis shows that a better combination of strength and ductility can be obtained by increasing the volume fraction of austenite within a certain range. While lowering the austenite stability will result in an increase in strength but at the same time a reduction in ductility.

In perspective, the proposed method can be used to guide the microstructure design of medium Mn steels to improve mechanical properties by optimizing the volume fraction and stability of austenite. It can also be applied to other multiphase materials, including those with metastable phases. Furthermore, the proposed method itself is expected to be improved by combining it with phase-level hardness assessment using advanced nano-indentation [53].

Data Availability The raw/processed data required to reproduce these findings cannot be shared at this time as the data also forms part of an ongoing study.

Declarations

Conflict of interest The authors declare that they have no known competing financial interests or personal relationships that could have appeared to influence the work reported in this paper.

References

1. D.W. Suh, S.J. Kim, Scripta Mater. **126**, 63–67 (2017)
2. O. Kwon, K.Y. Lee, G.S. Kim, K.G. Chin, Mater. Sci. Forum **638–642**, 136–141 (2010)
3. K.M.H. Bhadhon, X. Wang, J.R. McDermid, Mater. Sci. Eng. A **833**, 142563 (2022)
4. D.J. Magagnosc, D.M. Field, C.S. Meredith, K. An, T.R. Walter, K.R. Limmer, J.T. Lloyd, Acta Mater. **231**, 117864 (2022)
5. B.-G. Zhang, X.-M. Zhang, H.-B. Li, H.-T. Liu, Met. Mater. Int. **29**, 607–617 (2023)
6. S.H. Kim, J.H. Kim, J.H. Lee, D.-W. Suh, J.S. Lee, Met. Mater. Int. **28**, 2059–2067 (2022)
7. M. Huo, H. Xie, T. Zhang, L. Li, F. Lin, F. Chen, J. Liu, T. Yang, V. Linton, Z. Jiang, Met. Mater. Int. **29**, 1052–1066 (2023)
8. X. Wang, C. Liu, B. Sun, D. Ponge, C. Jiang, D. Raabe, Proc. Natl. Acad. Sci. **119**, e2110139119 (2022)
9. J. Han, Y.K. Lee, Acta Mater. **67**, 354–361 (2014)
10. W. Wang, Y. Liu, Z. Zhang, M. Yang, L. Zhou, J. Wang, P. Jiang, F. Yuan, X. Wu, J. Mater. Sci. Technol. **132**, 110–118 (2023)
11. D.P. Yang, P.J. Du, D. Wu, H.L. Yi, J. Mater. Sci. Technol. **75**, 205–215 (2021)
12. Z. Wang, M.X. Huang, Int. J. Plast. **134**, 102851 (2020)
13. A.K. Patra, C.N. Athreya, S. Mandal, K.C. Hari Kumar, V. Subramanya Sarma, Mater Sci. Eng. A **810**, 140756 (2021)
14. Y. Zhang, H. Ding, H. Zhu, X. Zhou, Y. Zhang, N. Jia, Mater. Sci. Eng. A **834**, 142443 (2022)
15. B.B. He, M.X. Huang, Z.Y. Liang, A.H.W. Ngan, H.W. Luo, J. Shi, W.Q. Cao, H. Dong, Scripta Mater. **69**, 215–218 (2013)
16. M. Kuzmina, M. Herbig, D. Ponge, S. Sandlöbes, D. Raabe, Science **349**, 1080–1083 (2015)
17. X. Zhang, S. Gai, T. Liu, Y. Shi, Y. Wang, Q. Zhou, Z. Xing, H. Liu, Z. Zhai, Mater. Charact. **197**, 112650 (2023)
18. B. Sun, N. Vanderesse, F. Fazeli, C. Scott, J. Chen, P. Bocher, M. Jahazi, S. Yue, Scripta Mater. **133**, 9–13 (2017)
19. X.G. Wang, L. Wang, M.X. Huang, Acta Mater. **124**, 17–29 (2017)
20. X.G. Wang, C.H. Liu, B.B. He, C. Jiang, M.X. Huang, Mater. Sci. Eng. A **761**, 138050 (2019)
21. B. Hu, H. Luo, F. Yang, H. Dong, J. Mater. Sci. Technol. **33**, 1457–1464 (2017)
22. T.T.T. Trang, Y.-U. Heo, Mater. Charact. **178**, 111264 (2021)
23. F. Yang, H. Luo, C. Hu, E. Pu, H. Dong, Mater. Sci. Eng. A **685**, 115–122 (2017)
24. I. Janeiro, O. Hubert, J.H. Schmitt, Int. J. Plast. **154**, 103248 (2022)
25. D.W. Suh, S.J. Park, T.H. Lee, C.S. Oh, S.J. Kim, Metall. Mater. Trans. A **41**, 397 (2009)
26. D.H. Kim, J.H. Kang, J.H. Ryu, S.J. Kim, Mater. Sci. Eng. A **774**, 138930 (2020)
27. M. Zhang, H. Chen, Y. Wang, S. Wang, R. Li, S. Li, Y.D. Wang, J. Mater. Sci. Technol. **35**, 1779–1786 (2019)
28. Q. Guo, H.W. Yen, H. Luo, S.P. Ringer, Acta Mater. **225**, 117601 (2022)
29. H. Kamoutsi, E. Gioti, G.N. Haidemenopoulos, Z. Cai, H. Ding, Metall. Mater. Trans. A **46**, 4841–4846 (2015)
30. D.H. Kim, J.H. Kang, H. Gwon, J.H. Ryu, S.J. Kim, J. Mater. Sci. Technol. **98**, 248–257 (2022)
31. P.J. Gibbs, B.C. De Cooman, D.W. Brown, B. Clausen, J.G. Schroth, M.J. Merwin, D.K. Matlock, Mater. Sci. Eng. A **609**, 323–333 (2014)
32. H.S. Oh, K. Biggs, O. Güvenç, H. Ghassemi-Armaki, N. Pottore, C.C. Tasan, Acta Mater. **215**, 117023 (2021)
33. J.H. Ryu, D.I. Kim, H.S. Kim, H.K.D.H. Bhadeshia, D.W. Suh, Scripta Mater. **63**, 297–299 (2010)
34. F. Zhao, P. Chen, B. Xu, Q. Yu, R.D.K. Misra, G. Wang, H. Yi, Mater. Charact. **179**, 111327 (2021)
35. B. Sun, F. Fazeli, C. Scott, X. Yan, Z. Liu, X. Qin, S. Yue, Scripta Mater. **130**, 49–53 (2017)
36. R. Cao, X. Yu, Z. Feng, W. Liu, R. Xu, M. Ojima, T. Koseki, Mater. Charact. **145**, 634–643 (2018)
37. S. Lee, B.C. De Cooman, Metall. Mater. Trans. A **45**, 709–716 (2014)
38. S. Lee, Y. Estrin, B.C. De Cooman, Metall. Mater. Trans. A **44**, 3136–3146 (2013)
39. E.J. Seo, L. Cho, Y. Estrin, B.C. De Cooman, Acta Mater. **113**, 124–139 (2016)
40. M.I. Latypov, S. Shin, B.C. De Cooman, H.S. Kim, Acta Mater. **108**, 219–228 (2016)

41. O. Bouaziz, P. Buessler, Rev. Metall. **99**, 71–77 (2002)
42. B.B. He, B. Hu, H.W. Yen, G.J. Cheng, Z.K. Wang, H.W. Luo, M.X. Huang, Science **357**, 1029–1032 (2017)
43. S.H. He, B.B. He, K.Y. Zhu, M.X. Huang, Acta Mater. **149**, 46–56 (2018)
44. S. Lee, B.C. De Cooman, Metall. Mater. Trans. A **45**, 6039–6052 (2014)
45. B.B. He, Z.Y. Liang, M.X. Huang, Scripta Mater. **150**, 134–138 (2018)
46. F. Yang, H. Luo, E. Pu, S. Zhang, H. Dong, Int. J. Plast. **103**, 188–202 (2018)
47. M. Callahan, A. Perlade, J.-H. Schmitt, Mater. Sci. Eng. A **754**, 140–151 (2019)
48. Z.Y. Liang, Z.H. Cao, J. Lu, M.X. Huang, C.C. Tasan, Acta Mater. **221**, 117418 (2021)
49. H. Wang, Y. Zhang, G. Yuan, J. Kang, Y. Wang, R.D.K. Misra, G. Wang, Mater. Sci. Eng. A **737**, 176–181 (2018)
50. F.D. Fischer, G. Reisner, E. Werner, K. Tanaka, G. Cailletaud, T. Antretter, Int. J. Plast. **16**, 723–748 (2000)
51. G.B. Olson, M. Cohen, Metall. Trans. A **6**, 791 (1975)
52. X.G. Wang, L. Wang, M.X. Huang, Mater. Sci. Eng. A **674**, 59–63 (2016)
53. K.I. Kim, Y. Oh, D.U. Kim, J.-H. Kang, N.I. Cho, K.H. Oh, J.-Y. Kang, H.N. Han, Met. Mater. Int. **28**, 1094–1104 (2022)